View metadata, citation and similar papers at core.ac.uk

brought to you by CORE

provided by Digital.CSIC

Alkoxide-based precursors for direct drawing of metal oxide micro- and nanofibres

This article has been downloaded from IOPscience. Please scroll down to see the full text article.

2011 Sci. Technol. Adv. Mater. 12 034412

(http://iopscience.iop.org/1468-6996/12/3/034412)

View the table of contents for this issue, or go to the journal homepage for more

Download details:
IP Address: 161.111.180.191
The article was downloaded on 28/03/2012 at 11:07

Please note that terms and conditions apply.

Sci. Technol. Adv. Mater. **12** (2011) 034412 (12pp) doi:10.1088/1468-6996/12/3/034412

Alkoxide-based precursors for direct drawing of metal oxide micro- and nanofibres

Tanel Tätte[1], Medhat Hussainov[1], Madis Paalo[1], Marko Part[1], Rasmus Talviste[1], Valter Kiisk[1], Hugo Mändar[1], Kaija Põhako[1], Tõnis Pehk[2], Kaido Reivelt[1], Marco Natali[3], Jonas Gurauskis[4], Ants Lõhmus[1] and Uno Mäeorg[5]

[1] Institute of Physics, University of Tartu, Riia 142, Tartu 51014, Estonia
[2] National Institute of Chemical and Biological Physics, Akadeemia tee 23, Tallinn 12618, Estonia
[3] ICIS-CNR, Corso Stati Uniti 4, Padova 35127, Italy
[4] Instituto de Ciencia de Materiales de Aragón C.S.I.C., University of Zaragoza Fac. De Ciencias, c/Pedro Cerbuna 12, Zaragoza 50009, Spain
[5] Institute of Chemistry, University of Tartu, Ravila 14a, Tartu 50411, Estonia

E-mail: tanelt@fi.tartu.ee

Received 10 January 2011
Accepted for publication 10 May 2011
Published 28 June 2011
Online at stacks.iop.org/STAM/12/034412

Abstract
The invention of electrospinning has solved the problem of producing micro- and nanoscaled metal oxide fibres in bulk quantities. However, until now no methods have been available for preparing a single nanofibre of a metal oxide. In this work, the direct drawing method was successfully applied to produce metal oxide (SnO_2, TiO_2, ZrO_2, HfO_2 and CeO_2) fibres with a high aspect ratio (up to 10 000) and a diameter as small as 200 nm. The sol–gel processing includes consumption of precursors obtained from alkoxides by aqueous or non-aqueous polymerization. Shear thinning of the precursors enables pulling a material into a fibre. This rheological behaviour can be explained by sliding of particles owing to external forces. Transmission (propagation) of light along microscaled fibres and their excellent surface morphology suggest that metal oxide nanofibres can be directly drawn from sol precursors for use in integrated photonic systems.

Keywords: oxide nanofibres, microfibres, sol–gel, metal alkoxides, rheology, SAXS, SnO_2

1. Introduction

Metal oxide micro- and nanofibres have numerous technical applications in textiles, matte filters, optical cables, thermal insulators, reinforcing components, etc. These and other, expanding applications are keeping researchers active in developing novel fibre preparation technologies.

Fibres are traditionally prepared using a top–down approach such as drawing filaments from viscous liquid precursors and applying external forces to stretch the precursors into fibres. This is a typical chemical technology process where the precursor properties are crucial. The main demand for the precursors is spinnability, defined as the ability of liquid to form threads under application of external stress, mechanical or electrostatic (electrospinning) forces [1]. The second requirement is the possibility to transform viscous precursor jets into solid fibres, which is usually achieved via drying (dry pulling), cooling (melt pulling), osmosis (wet pulling) or as a result of chemical reactions [1, 2]. Drawing of viscous jets naturally proceeds until failure of the thread. The phenomenon, also known as pinching off the jets, is important in the formation of liquid drops and has found use in direct drawing of sharp needles [3]. The factors leading to failure are summarized in the Ullman's Fibers Handbook [1] as follows: A fluid as-spun filament is thought to break by two mechanisms [4]. The first of these is cohesive failure

 © 2011 National Institute for Materials Science Printed in the UK

in which fracture occurs when the tensile stress exceeds the tensile strength of the material at some point along the path of filament formation. Tensile strength depends on the energy of cohesion (critical elastic energy) of the material. Tensile stress can built up if the fluid, in contrast to ideal viscous Newtonian media is able to store energy of deformation, i.e. if it is viscoelastic. The second failure mechanism is termed capillary wave failure and depends on the ratio of surface tension to viscosity. The larger the ratio, the more rapid is increase in the amplitude of initially minute waves on the filament surface. After a certain distance, the capillary filament is divided into droplets and breaks. In order to prepare continuous fibres, the solidification should be quick enough to prevent the break-up of the jet.

Because of the break-up, it is rather difficult to draw fibres thinner than 1 μm. The fundamental diameter limit of the current mechanical drawing methods is estimated as 200 nm [5]. The use of electrostatic forces, which harness non-locally over the whole length of the jet, in combination with volume shrinking due to solvent evaporation, has been proposed to overcome this diameter limit. Methods such as electrospinning allow drawing fibres with diameters even less than 100 nm [6]. The technology is highly productive and suitable for preparing fibres as mattes applicable for ultrafiltration, composites, medical materials, textiles, etc [7].

The drawing of ceramic fibres had attracted great attention during the 1980 s [8, 9] because it allowed producing temperature-resistant and mechanically stable textiles and fibrous materials. Metal oxides rather decompose upon heating than transform into viscous melts, and therefore the key to the preparation of metal oxide fibres is finding suitable precursors. Metal-oxide-organic materials such as metal alkoxides have been exploited for that purpose, because it is possible to chemically adjust their most important parameters: reactivity and viscoelasticity. The desired range of viscosity from a hundred to some thousand poises is achieved by condensation of the compounds, which could be initiated by addition of water or by thermal treatment [8].

Until very recently, the two-step hydrolysis-polycondensation mechanism was mostly used to explain the reactivity of alkoxides under water treatment [10, 11]; however, the mechanism that explains well the behaviour of silicon (non-metal) alkoxides is still inadequate for metal alkoxides. A more appropriate concept for metal alkoxides was recently suggested and proven by the group of V Kessler [12]. It considers metal alkoxides as Lewis acids that undergo one-step polycondensation as soon as water is added. Well-defined oligonuclear oxo-alkoxide species form in this process [13]. Non-aqueous (NAQ) condensation—the Bradly's reaction—proceeds by ether elimination at elevated temperatures [14, 15].

Whereas the aqueous (AQ) approach is a conventional chemical process and the basis of the sol–gel technology [16–18], the NAQ thermal process has been almost forgotten since some early works [19–21]. These two different chemical approaches yield a rather similar product: metal-oxo-alkoxides—small, (partially) crystalline, nanometre-sized oxide nanoparticles stabilized by a shell of alkoxy groups. Recently the NAQ process has been rediscovered and applied for growing metal oxide nanoparticles [14, 15].

Sakka and Yoko have proved on silicon alkoxides based systems that only solutions of linearly shaped polymeric particles can be spun into fibres [8]. They have also showed that acidic reaction conditions during polymerization are required for synthesizing elongated particles. During the fibre processing the precursor particles start sliding under external forces, forming long slender viscous jets that solidify (gel) upon removal of the solvent and cross-linkage of the particles.

Most applications need oxides as stable, dense and organics-free ceramics, and thus the preparation of gel-fibres is usually just an initial step. The goal—synthesis of pure crystalline oxide material—is achieved as a result of ageing, heating, laser treatment [22], UV-light treatment, etc [17]. In the first stage of heating the organic component is removed and the pores of the material collapse as a result of sintering. In the temperature range of 300–400 °C the residual carbon oxidizes, and at higher temperatures the materials crystallize. The disadvantages of the sol–gel method include blackening (due to the formation of free carbon), cracking and a decrease in the optical transparency, among others. To overcome these problems, it is suggested that the product should be less bulky, freestanding, more symmetric and homogeneous [23, 24].

Electrospinning enables mass production of fibres and is not suited for the preparation of single fibres in a desired position. Therefore, for applications requiring a single fibre the fibre should be selected out from the bundle and manipulated with a tip of a scanning probe microscope, optical tweezers or other delicate and expensive manipulators.

To overcome this drawback and prepare single nanofibres of desired dimensions at a certain position on a substrate, the direct drawing—probably the oldest known pulling technique—has been improved. Fibres thinner than 200 nm were prepared by Ondarçuhu who used concentrated oligomeric precursor solutions instead of polymer solutions [5]. The advantage of these solutions is related to the absence of entanglements in oligomeric systems with low molecular mass, so that the cohesive forces are largely reduced. Another system used to directly draw single nanofibres is silica glass. In this case, precise control over the material homogeneity is achieved by thermostation of the silica melt at 2000 K, and fibres can be prepared with a diameter as small as tens of nanometres [25]. Fibres obtained by this method have a perfectly smooth surface, ultrahigh homogeneity, round cross section and high aspect ratio ($\sim$10 000). Recently, automatic processes have been suggested for direct drawing of fibres to connect points on solid substrates [26]. Although this enables drawing of fibres as thin as 37 nm, the technology is demonstrated only for polymer fibres. In the case of ceramics, direct drawing of fibres has resulted in diameters of tens of microns [9]. It should be noted that anisotropic crystal growth alternatively enables bottom-up approach for preparation of metal oxide nanofibres and 1D structures [27–29]. Because of the specific growth, the materials are produced in the form of multiple monocrystalline needles or belts. Initiation of the growth of one crystal is usually a complex task.

In this paper, we report the limitations of direct drawing of metal alkoxide concentrates into metal oxide (TiO_2, SnO_2, ZrO_2, HfO_2, CeO_2, etc) fibres. Precursors were obtained from propoxides and butoxides of the corresponding metals as a result of AQ or NAQ treatments. Suitable rheological properties of the AQ precursors were obtained by concentrating their solutions in vacuum. Solventless precursor materials were stable for one year in dry atmosphere at room temperature. The alkoxide precursors prepared with the NAQ treatment have earlier found almost no use in materials processing, but showed the best performance in our experiments; therefore, this study describes the processing and structure of these materials in detail. The preparation and properties of the precursors were studied by thermogravimetry, rheological analysis, Fourier-transform infrared (FTIR) spectroscopy, ^{119}Sn nuclear magnetic resonance (NMR) and small-angle x-ray scattering (SAXS). This article is based on the comparison and discussion of the NAQ and AQ precursor processing and the resulting different properties as key factors in the fibre drawing. From the NAQ precursors with the best rheological properties among the materials described we could directly draw fibres with a diameter as low as 200 nm and an aspect ratios up to 10 000. The processing was carried out by simple manipulations at ambient conditions. The final fibres were heat-treated at 550 °C and characterized by x-ray diffraction (XRD), atomic force microscopy (AFM), scanning electron microscopy (SEM) and optical waveguiding measurements.

2. Experimental details

2.1. Neat alkoxides for precursor preparation

$Ti(OPr)_4$, $Ti(OBu)_4$, $Zr(OPr)_4$, $Zr(OBu)_4$ and $Hf(OBu)_4$ were purchased from the Sigma-Aldrich company.

Synthesis of $Sn(OPr)_4$ and $Sn(OBu)_4$ was carried out as described in [30]. After removal of solvents in vacuum, the alkoxides were obtained as viscous maple syrup-like brown liquids. They were characterized by FTIR spectroscopy and thermogravimetry. Rheological tests were carried out for $Sn(OBu)_4$.

$Ce(OBu)_4$ was synthesized as described in [31]. Gaseous NH_3 was let flow over the solution of 100 g of cerium(IV)ammonium nitrate in 200 g methanol and 200 g butanol for 30 min. During the first 5 min the colour of the solution almost bleached. After NH_3 treatment the solution was aged for 24 h. A saturated amine complex was separated by vacuum filtration. For preparing homogeneously viscous and suitable for fibre drawing materials it was necessary to filter off even the traces of the complex. To achieve that the alkoxide was concentrated in vacuum and then dissolved in pentane. The precipitate that formed in the solution was filtered off. After the concentration, the alkoxides were tested for fibre drawing, and the purification process was repeated until no more precipitate was formed. The final product (20–30% yield) was directly used for fibre drawing after removal of all the solvent in vacuum (5 Torr) on a water bath (70 °C).

2.2. Precursor preparation

2.2.1. AQ oligomerization of metal alkoxides. Five grams of alkoxide aliquots was used as the starting material for the precursor preparation. Oligomerization was initiated by adding water to form 5% solution in the corresponding alcohol (butanol or propanol) acidified with ∼20 mg of concentrated (∼35%) aqueous solution of HCl. To transform the obtained mixtures into viscous fibre-drawing dopes, the solvents and low molecular mass organics were removed by evacuation (1–2 Torr) and heating to 70 °C on a water bath.

The viscosity dependence on the water/alkoxide molar ratio R was studied using the Stokes method. A detailed rheological analysis was carried out for $Sn(OBu)_4$-based samples obtained at a mole ratio $R = 0.7$, which was optimal for the fibre drawing.

2.2.2. NAQ (thermolysis) oligomerization of $Sn(OBu)_4$. For thermolysis, 40 g of $Sn(OBu)_4$ was taken into a 100 ml reaction flask. Condensation was initiated by slowly increasing the temperature over an 8 h period until reaching 275 °C, at which temperature primary tin alkoxides finally transform to oxides, as pointed out by Maire [32].

To achieve uniform heating, the flask with a vigorously stirred substance was heated on a silicone oil bath. In order to remove volatile organics during the experiment, the flask was evacuated to 1–5 Torr with two 2-stage membrane pumps (V900, Büchi). The temperature was feedback-controlled to maintain boiling caused by the release of low boiling-point organics, which continued for ∼8 h. Evacuated gases were trapped into a condenser cooled down to the liquid nitrogen temperature. After each removal of around 5–10% of the substance mass, the flask was flushed with dry argon and the reaction was stopped for approximately 3 min for taking out the precursor samples. As a result of the experiment 2–3 g of the aliquots of 7 potential precursors (fractions 1–7) were prepared and sealed into plastic syringes for further analysis and fibre drawing experiments.

All the fractions were analysed by thermogravimetry, and the mass loss curve was constructed from the obtained results (figure 3) to describe the decomposition of $Sn(OBu)_4$·xBuOH. The deviation of the final point (at ∼270 °C) from the general trend could be explained by inhomogeneities due to the difficulty in stirring the highly viscous liquid. Rheological measurements were carried out for the fraction 5 which had the best fibre drawing properties.

2.3. Characterization of the precursor

2.3.1. Thermogravimetry. Thermogravimetric analysis was carried out to measure the solid fraction of pure alkoxides of tin and titanium as well as precursors obtained by the NAQ thermal treatment. The samples were weighed, aged for 2 days and then heat-treated for 1 h at 900 °C to transform the materials into tetravalent metal oxides.

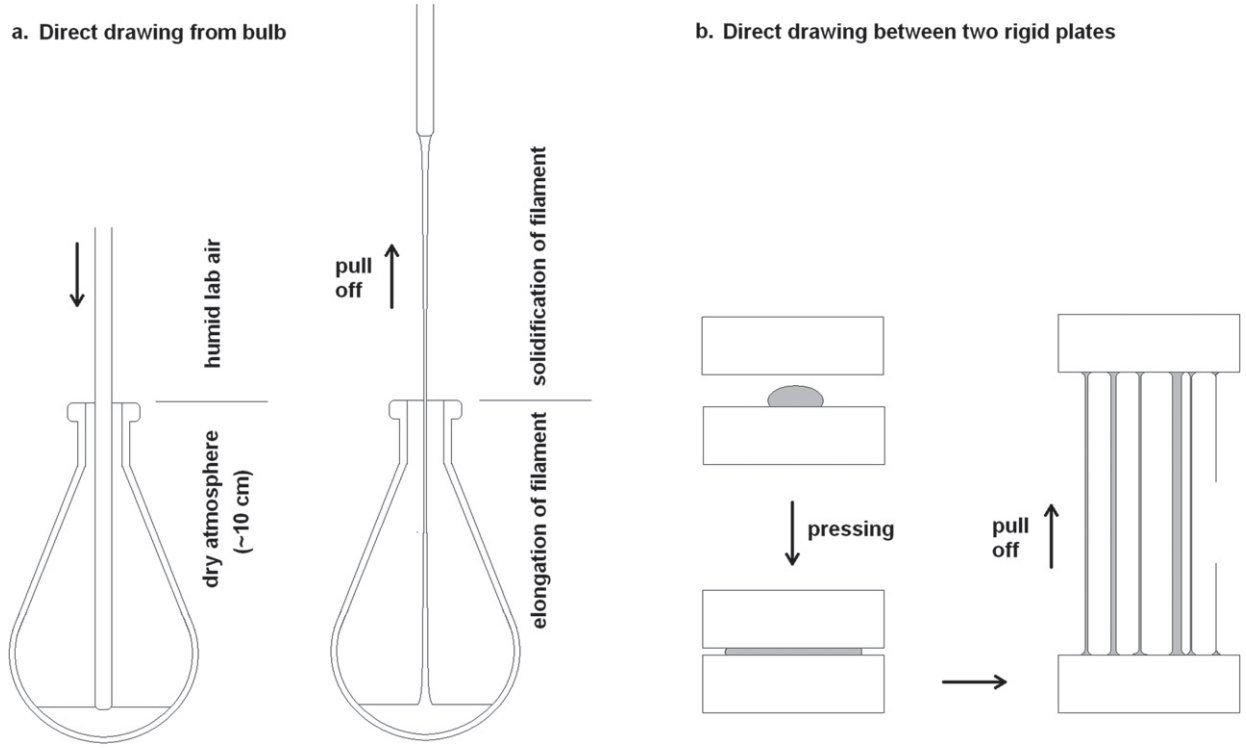

Figure 1. Principles of fibre drawing: (a) from dry atmosphere in the flask into humid atmosphere and (b) in humid atmosphere.

2.3.2. Viscosity measurements. Viscosity of the precursors was measured by Stokes method using 32 mg polished stainless steel metal balls. Measurements were performed after concentration of the material in 1–2 Torr vacuum until boiling stopped. The calibration of the method using the Paragon Limited viscosity standards S600, S8000 and S30000 proved 10% accuracy.

2.3.3. Rheological characterization. The rheological characterization of samples was carried out with a rotational rheometer Mars II (Haake, Karlsruhe, Germany), in the plate-and-plate test geometry (plate diameter 20 mm), at $20 \pm 0.1\,^{\circ}$C and humidity below 20%.

The data on viscosity versus shear rate were averaged over 30 s for each shear rate value. Oscillation stress sweep tests were carried out at a frequency of 10 rad s^{-1} and a strain amplitude of 0–30%. Oscillation frequency sweep tests were performed for frequencies between 0.01 and 20 Hz at the strain amplitude of 0.1%, that is, within the linear viscoelastic region.

2.3.4. Measurements of the surface tension coefficient. The surface tension coefficient was measured by the inverted vertical pull surface tension method as described in [33]. To avoid the solidification of the sample surface, the measurements were performed inside the reaction flask in which alkoxide materials were in equilibrium with their vapours and where all humidity was consumed by the sample. A platinum rod, 0.5 mm in diameter, was immersed into the liquid, and the force of the liquid acting on the rod in a steady-state motion was measured using balances with a resolution of 0.1 mg. The rod was pulled out from the liquid in 0.01 mm steps, and the surface tension coefficient was calculated from the value of the force measured immediately before breaking up of the liquid jet. The method was calibrated in the high-viscosity region using standard liquids (glycerol, motor oil 5W-40, gear oil 75W-90), and the accuracy was within 5%.

2.3.5. SAXS measurements. SAXS spectra of $Sn(OBu)_4$-based precursors were recorded in the scattering vector range 0.07–5.3 nm^{-1}, using a slit collimation camera KRM-1 (sample to detector distance was 250 mm), Cu K_α radiation and a NaI:Tl scintillation detector. The beam path was kept in a 0.1 mbar vacuum. Samples were sealed into 1.5 mm diameter fused-end Mark capillaries. An advanced version of the program AXES [34] was used for smoothing the data and preparing data files for the software system SYRENA [35], which takes into account spurious and buffer scattering and performs desmearing. The program ATSAS [36] was used for calculating the radius of gyration R_g and for 3D modelling of the cluster shape.

2.3.6. FTIR measurements. The spectra were recorded with a Nicolet 6700 spectrometer equipped with CsI optics, DLaTGS detector and a micro-ATR sampling accessory with a diamond crystal allowing to extend the range down to 225 cm^{-1}. To avoid the alkoxide hydrolysis the samples were kept in syringes in a dry box and pressed directly on the ATR crystal just before the measurement. No humidity effects could be detected, although the measurements were performed in an ambient atmosphere.

2.3.7. NMR measurements. ^{118}Sn, ^{13}C and ^{2}H NMR spectra were recorded with a Bruker AMX 500 FT NMR instrument using $CDCl_3$ as the solvent and tetramethyl tin as the external standard.

2.3.8. XRD measurements of $Sn(OBu)_4$. XRD diffraction patterns were recorded with a Philips PW3020 Bragg–Brentano powder diffractometer using Cu K_α radiation and the 2θ-ω scanning mode. Liquid or powder samples were loaded into Lindemann glass capillaries (0.1 mm wall thickness, 1 mm diameter) in a dry-atmosphere glovebox. To avoid humidity effects during the measurements, the ends of the capillaries were fused. Crystalline phases were identified by comparing the peaks with the data from the JCPDS-ICDD database.

2.4. Fibre drawing

The fibres were directly drawn from the concentrates using two different procedures.

2.4.1. Pulling from dry to humid atmosphere. A glass rod with a round end and a 5 mm diameter was immersed to a 1 mm depth in a 5 g volume of a precursor placed in a 100 ml conical flask. Filaments followed the rod as viscous jets when the rod was pulled out from the flask at a constant speed of 0.1–3 m s^{-1}. In the first stage, the pulling was carried out in the flask where, owing to dry atmosphere, no surface solidification occurred, which is a characteristic feature of the method.

2.4.2. Pulling in humid atmosphere. A 10–20 mg drop of precursor was pressed between two glass plates to form a 1 cm^2 spot that was achieved with a 100–200 μm spacing between the plates. Then the plates were pulled apart at a speed of 0.1–3 m s^{-1}. This method differs from direct drawing from the flask in that the jets are exposed to humid air all the time.

2.4.3. Ageing and heating. As-prepared fibres were aged for 1 week under normal lab conditions (relative air humidity 30–40%). Finally, the samples were baked at 550 °C for 6 h.

2.5. Characterization of the fibres

2.5.1. Microscopy. AFM images were acquired with a SMENA-B instrument (NTMDT) operated in the intermittent contact mode with NSG11 cantilevers (NTMDT). SEM images were taken with a LEO 1430 VP microscope.

2.5.2. Evaluation of microfibres as optical waveguides. Optical losses in the fibres were evaluated by examining, under an optical microscope (Carl Zeiss Axioskop 2) equipped with a 20× long-distance objective, the lateral scattering of 532 nm laser light propagating through the fibre. Micrographs of the radiant intensity distribution along the fibre were acquired with a Scion CFW-1612C digital camera.

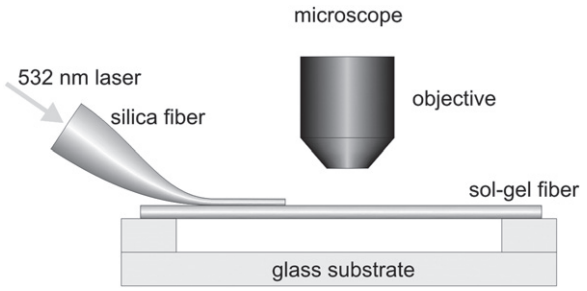

Figure 2. The setup used for the evaluation of optical losses in the sol–gel-prepared fibres.

For evanescent coupling, the laser beam was introduced into a conventional 50 μm core silica fibre whose tapered-down end (∼1 μm diameter) was brought into contact with a freestanding sol–.gel-prepared fibre supported at both ends (figure 2). The coupling scheme is similar to that used previously for the investigation of various glass and semiconductor nanowires [37, 38].

3. Results and discussion

3.1. Alkoxides

All neat alkoxides used in this study were viscous, maple syrup-like liquids sensitive to humidity. Thermogravimetric analysis showed that commercial $Ti(OBu)_4$ and $Ti(OPr)_4$ do not contain any solvated alcohols. The synthesized $Sn(OBu)_4$ and $Sn(OPr)_4$ samples contained 6–7 wt% of solvated alcohols (∼1 alcohol molecule per 2 alkoxide molecules).

The viscous nature of neat alkoxides is notable as it distinguishes primary alkoxides (ethoxides, propoxides, butoxides, etc) of metals (Ti, Zr, Hf, Sn, Ce, etc) from their silicon analogues and from secondary and tertiary alkoxides of these metals, which have a viscosity lower by several orders of magnitude. This property is explained by the extremely high acidity of metal alkoxides in the Lewis sense, that is the driving force of self-agglomeration [12, 13]. Abnormal behaviour of these alkoxides was noticed by Bradly who during the 1950 s proved, using cryoscopic and ebullioscopic molar mass detection methods, that these compounds exist as trimers or tetramers rather than monomers [39]. Viscosity depends on the particle size [40] and increases upon agglomeration [41]. Single-crystal x-ray structure analysis became a routine method two decades later. Since then, detailed structure analyses of a wide variety of secondary alkoxides were carried out [42]. However, x-ray structure identification studies have been relatively rare for primary alkoxides, because sufficiently large monocrystals can be grown only for methoxides and ethoxides of some metals [42]. Structure analyses have proved that alkoxide agglomerates are usually solvated by alcohol molecules, which act as Lewis bases [42].

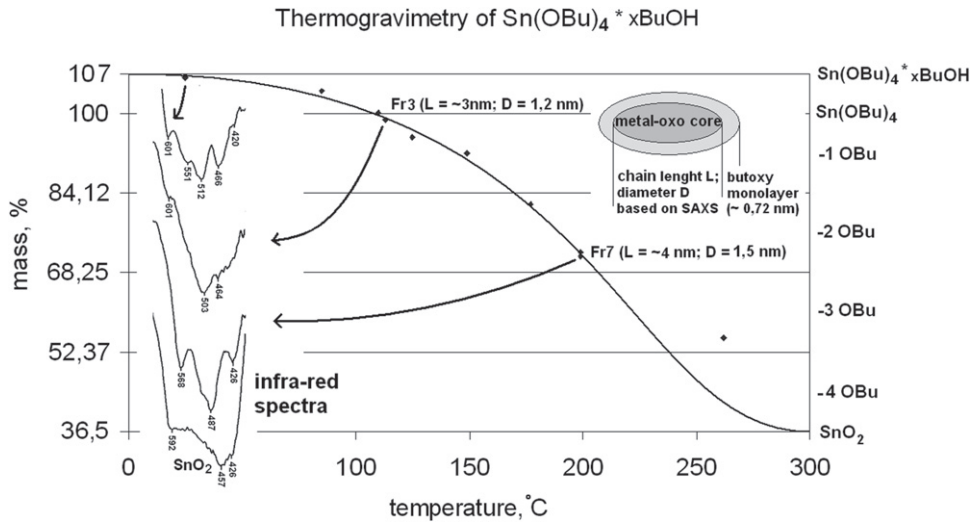

Figure 3. Thermogravimetry curves of $Sn(OBu)_4$. The evolution of the chemical structure during the measurement is indicated on the right Y-axis where -1 OBu, -2 OBu, etc, denote numbers of eliminated butoxy groups per $Sn(OBu)_4$. The starting point on the left Y-axis has been set at 107% because the sample contained 7 wt% of solvated butanol. The FTIR spectra show the range of the Sn–O-skeletal vibrations.

Table 1. Water/alkoxide molar ratios in the precursors used for fibre drawing.

Alkoxide	R
$Sn(OBu)_4$	0.5–0.8
$Sn(OPr)_4$	0.2–0.3 (decomp.)
$Ti(OBu)_4$	0.6–0.9
$Ti(OPr)_4$	0.5–0.8
$Zr(OBu)_4$	0.4–0.6
$Zr(OPr)_4$	0.4–0.6
$Hf(OBu)_4$	0.4–0.6
$Ce(OBu)_4$	0
$Ce(OPr)_4$	0

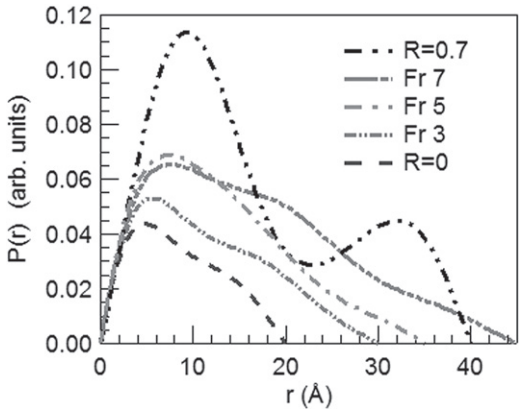

Figure 4. SAXS pair distribution functions $P(r)$ of the AQ and NAQ samples prepared from $Sn(OBu)_4$ precursors, measured as 10% solutions in hexane. Fr. 3, Fr. 5 and Fr. 7 mark fractions of the NAQ-treated $Sn(OBu)_4$. $R = 0.7$ is the mole ratio of the AQ-treated $Sn(OBu)_4$ sample.

3.2. Preparation and chemistry of precursors

In this work both AQ and NAQ methods were applied to grow the corresponding metal-oxo-alkoxide nanoclusters in case of $Sn(OBu)_4$. The AQ approach resulted in optimal spinnability if 0.7 mole of water was added to one mole of $Sn(OBu)_4$ (water/alkoxide mole ratio $R = 0.7$). Suitable R-values for other studied alkoxide systems are presented in table 1. Spinnability was achieved after concentrating the obtained solutions in vacuum. In the NAQ case, the fibre drawing was optimal after $Sn(OBu)_4$ was heat-treated at 170 °C in a vacuum of 1 Torr (fraction 5). The thermogravimetry curve of $Sn(OBu)_4$ that is based on the solid content analysis of each fraction (figure 3) fits well to the earlier data [32].

The SAXS pair distribution functions (figure 4) and DAMMIN modelling of the scattering patterns of $Sn(OBu)_4$-based samples suggested that the particles have elongated shapes, with a 3.5–4.5 nm length and 1.2–1.6 nm diameter for both AQ ($R = 0.7$) and NAQ (fraction 5) precursors, which appeared the optimum values for fibre drawing. Metal oxo-alkoxides are known to consist of nanospheres [12, 13, 42], and thus the elongated shape can be explained by the formation of secondary particles. Such behaviour of metal alkoxides is well known and could finally lead to the formation of a 3D solid network and gelation [12, 13]. NAQ fraction 3 contained clusters up to 2 nm in length. Pure $Sn(OBu)_4$ is known to exist as a mixture of trimers and tetramers [39, 42] arranged in particles 0.9 nm in diameter and 2 nm in length.

XRD analysis did not detect any crystalline phases in the case of AQ-prepared precursors. The NAQ sample fraction 6 showed broad reflections at $2\theta \sim 25°$, 54° and 85° (figure 5). By interpolation, using the Bragg equation for these reflections, they can be assigned to the same set of lattice planes with the interplanar distance $d = 3.36$ Å. This value agrees well with the spacing of $d = 3.35$ Å between the cassiterite (110) planes. A simulation based on Debye function was performed to verify the presence of cassiterite and estimation of its crystallite size. This simulation allows calculating the diffraction and scattering x-ray patterns from particles of any size, shape and internal structure. We have assumed spherical SnO_2 (cassiterite) particles and calculated XRD patterns for diameters between 0.5 and 5 nm. The

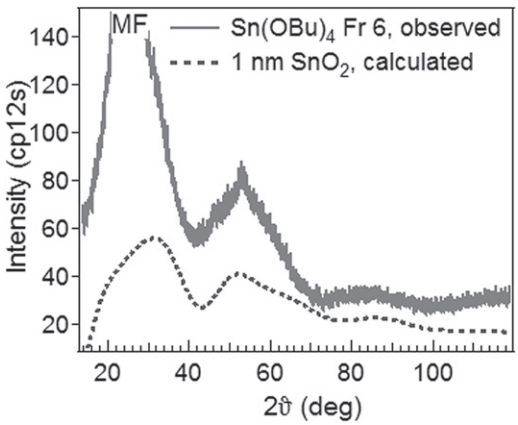

Figure 5. Observed XRD pattern (solid curve) from the NAQ $Sn(OBu)_4$ precursor (fraction 6) and a pattern calculated with the Debye function (dotted curve) for a spherical 1 nm SnO_2 (cassiterite) particle.

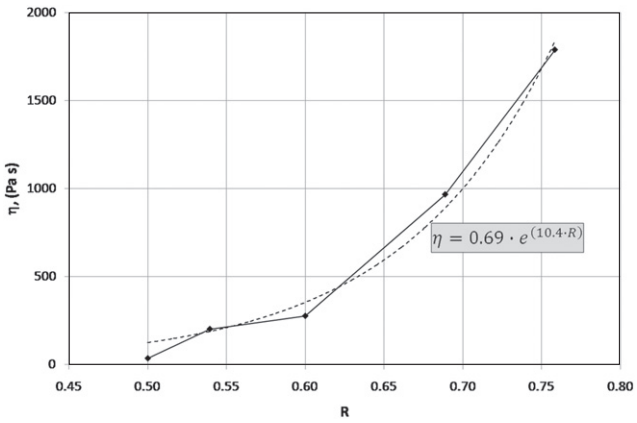

Figure 6. Dependence of the viscosity η of $Sn(OBu)_4$ AQ concentrates on the water/alkoxide mole ratio R. The viscosities were measured after concentration of the precursors in vacuum.

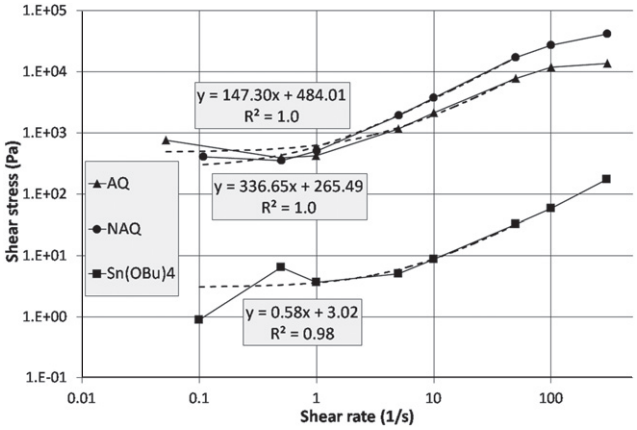

Figure 7. Shear stress versus shear rate for $Sn(OBu)_4$ systems. Dashed lines show the fit by the Bingham model.

best agreement with the experimental data was achieved for 1 nm particles (figure 5). The difference at angles below 40° is caused by a strong contribution from Mylar foil. This result agrees well with the outer shape of $Sn(OBu)_4$ particles deduced from the SAXS analysis. The elongated particles detected by SAXS probably consist of two to four spherical particles merged in one direction. The internal structure of the primary spherical particles has some short-range order that corresponds to the structure of cassiterite. Crystallization of SnO_2 nanoparticles during the NAQ treatment could be explained by the tendency of metal oxides to self-crystallize, which in many cases could occur even at room temperature owing to the low enthalpy of crystallization [43].

FTIR analysis reveals growth of the 465 cm^{-1} peak associated with Sn−O vibrations during the AQ treatment of $Sn(OBu)_4$. $Sn(OBu)_4$ and its vacuum-concentrated products did not show any peaks in the 3300–3500 cm^{-1} range, which otherwise could be attributed to free-OH (non-ligated) stretching vibrations. The non-detection of the −OH stretching modes of the solvated butanol molecules could be explained by the peak broadening due to strong interactions with the metallic centre and by the low concentration of butanol (5–7 wt%).

FTIR spectra of the NAQ precursors showed characteristic changes in the 400–600 cm^{-1} range, which corresponds to the Sn–O stretching vibrations. The $Sn(OBu)_4$ spectrum has 5 distinguishable peaks with maxima at 420, 466, 512, 551 and 601 cm^{-1}, revealing a well-defined alkoxide structure. During the first annealing stage these peaks transformed into a broad band. Appearance of distinct peaks at 568, 487 and 426 cm^{-1} after heating above 170 °C proved formation of another well-defined structure.

Similar tendencies were noticed in the ^{119}Sn NMR spectra (figure 4). Neat $Sn(OBu)_4$ has 7 clearly distinguishable peaks between −629 and −605 ppm, which can be attributed to 6-coordinated Sn [44]. Moderately heated samples (fraction 3) show only one broad band in the same region. The samples heated to 170 °C and above (fractions 5–7) had additional broad signals between −470 and −350 ppm, which can be attributed to 5-coordinated Sn [44].

The sharp FTIR and ^{119}Sn NMR peaks belong to trimeric or tetrameric butoxy clusters of pure $Sn(OBu)_4$ having well-defined inter- and intramolecular structures [44]. The transformation of these peaks into a broad band in the first stages of heating at temperatures up to 130 °C could be explained by the release of solvated butanol, which vacated the coordination sites of Sn. Formation of new intermolecular bonds resulted in an irregular structure corresponding to the broad band; these stronger intermolecular forces also increased the viscosity. The viscosity decreased again upon heating to 150 °C and above. The appearance of clearly distinguishable FTIR peaks in this temperature range reveals the formation of another well-ordered structure, and the similarity of the peak positions in the region of Sn–O vibrations for the fractions 5–7 and SnO_2 suggests that this structure is based on metal oxide. This observation is supported by the XRD measurements that identify the cassiterite structure. The decreased coordination number leads to a lower viscosity as a result of the diminished ability to form intermolecular bonds.

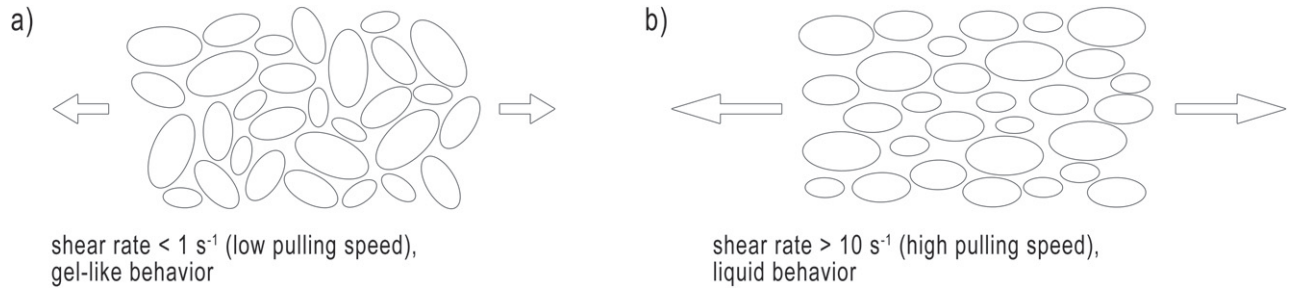

Figure 8. Aligment of elongated particles by external forces.

Table 2. Bingham model parameters for the $Sn(OBu)_4$ systems.

Sample	η (Pa s)	τ_y (Pa)
$Sn(OBu)_4$	0.58	3.02
AQ-treated	147.3	484.01
NAQ-treated	336.65	265.49

3.3. Effect of rheological properties and surface tension of precursors on fibre drawing

The exponentially rising curve in figure 6 shows the dependence of the viscosity η of the $Sn(OBu)_4$ system on the water/alkoxide mole ratio R used to induce condensation. The viscosities of other alkoxide systems in this study followed the same basic tendency. However, the concentrates of $Ce(OR)_4$ were spinnable as prepared. The $Ti(OPr)_4$ system formed precipitates at $R \geqslant 0.85$, and $Sn(OPr)_4$ slowly decomposed already at room temperature (boiling did not stop even after 1 h of evacuation). The nearly exponential growth of viscosity with R could be related to the increase of the particle size [39].

More detailed rheological studies were carried out for AQ (mole ratio $R = 0.7$) and NAQ-treated (fraction 5) products of $Sn(OBu)_4$, which showed the best fibre drawing properties.

As shown in figure 7, the shear stress–strain (τ–$\dot{\gamma}$) curves show a Bingham pseudoplastic behaviour of pronounced yield stress τ_y for the condensed liquids. The values of the parameters in the Bingham model, which can be written as $\tau = \tau_y + \eta \cdot \dot{\gamma}$, for the shear rates between 0.1 and 50 s^{-1} are listed in table 2.

Schematic explanation of the viscosity dependence on the shear rate is presented in figure 8. We suggest that the as-synthesized and AQ or NAQ-treated $Sn(OBu)_4$ exhibit a typical behaviour of non-Newtonian liquids. For all liquids the apparent dynamic viscosity decrease with the shearing rate, which is typical for polymeric liquids and can be explained by the alignment and sliding of elongated particles under applied stress (figure 9).

As-prepared $Sn(OBu)_4$ has a pronounced zero-shear plateau and shear thinning, which can be described by the Cross model as follows:

$$\eta = \frac{\eta_0 + \eta_\infty \cdot (K \cdot \dot{\gamma})^m}{(K \cdot \dot{\gamma})^m + 1}.$$

Here η_0 and η_∞ are zero and infinite shear viscosity and m and K are the Cross rate and Cross time constants, respectively; m reflects the degree of shear thinning, while

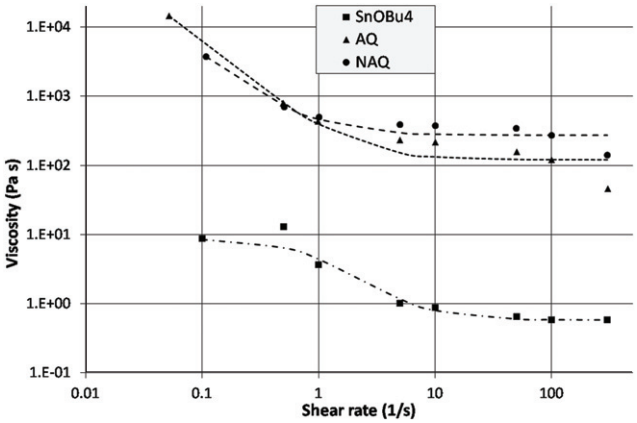

Figure 9. Viscosity of $Sn(OBu)_4$ systems plotted versus the shear rate.

Table 3. Sisko model parameters for the $Sn(OBu)_4$ systems.

Sample	η_0(Pa s)	η_∞ (Pa s)	K (s)	m
$Sn(OBu)_4$	8.8	0.6	1.1	1.5
AQ polymerized	14 500	120	19.33	1.37
NAQ polymerized	3738	273	9.82	1.30

$1/K$ indicates an onset shear rate of the shear thinning. The viscosity dependence on the shear rate for polymerized liquids is described by the Sisko model, which is relevant for structured liquids and can be expressed as follows:

$$\eta = \eta_\infty + \frac{\eta_0}{(K \cdot \dot{\gamma})^m}.$$

The values of the model parameters are given in table 3 for the studied liquids.

Constant viscosity values of 0.58, 121 and 273 Pa s for as-synthesized, AQ and NAQ polymerized $Sn(OBu)_4$ were obtained at shear rates of 100 s^{-1} and higher. The viscosities were two times higher for NAQ-processed than AQ-processed samples at high shear rates, and the shear thinning behaviour (m value) was more pronounced for the AQ samples.

Oscillatory measurements of viscous and elastic properties were performed to characterize the rheological state of the alkoxide systems. Firstly, the storage modulus G' (elastic response) was measured at a frequency of 10 rad s^{-1} to determine the linear viscoelastic region where the inner structure of a liquid remains intact. Figure 10 shows that NAQ-treated $Sn(OBu)_4$ has the widest linear viscoelastic

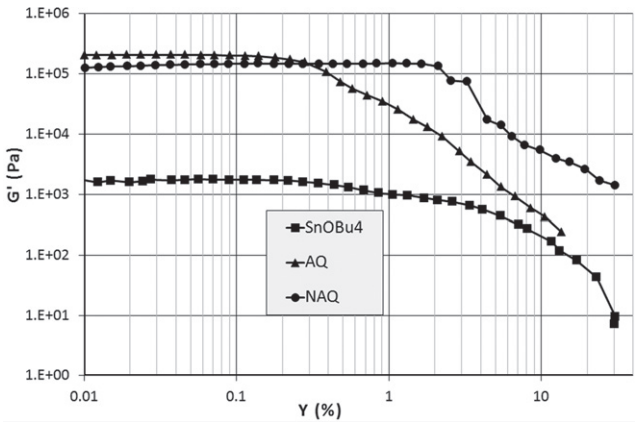

Figure 10. Determination of the linear viscoelastic limit for $Sn(OBu)_4$ systems: dependence of the storage modulus G' on strain amplitude Y at a frequency of 10 rad s^{-1}.

region. Breakdown of the network occurs at the strain amplitude higher than 2%. Initial and AQ-treated $Sn(OBu)_4$ have roughly the same linear viscoelastic region of the stable network up to 0.2% strain amplitude.

Figure 11 shows the frequency sweep results for the tin alkoxide systems at a strain amplitude of 0.1% (within the linear viscoelastic region). All the samples have a higher storage G' modulus (elastic response) than loss G'' modulus (viscous response) indicating a predominantly elastic behaviour. The frequency dependence of the moduli is polynomial for both the AQ and NAQ-processed systems; the power exponents of G' for the AQ and NAQ samples are 0.14 and 0.03, respectively, and both exponents are 0.15 for G''. A low value of the G' exponent indicates higher elasticity [45], thus the intermolecular cross-links are stronger for the NAQ than AQ precursor. The crossover point between G' and η^* indicates that the particle weight is larger for the NAQ than AQ samples at similar particle weight distributions.

Fibre formation is affected by the surface tension, and therefore the surface tension coefficients were measured for the studied liquids. The initial, AQ and NAQ-prepared $Sn(OBu)_4$ samples had the corresponding values at 26.6, 32.7 and 18.0 mN m^{-1}. The higher value for the AQ-treated samples can be explained by stronger intermolecular forces in their precursors. Note that the rheology analysis indicated higher elasticity for the NAQ-prepared precursors. Thus the surface tension measurements suggest different properties at the surface and in the bulk of the liquid phase, probably due to the contact with the atmosphere saturated with alcohol vapours. We suggest that the strength of the forces between the precursor particles depends mostly on the nature of their oxide cores. Sn centres at the surface of denser NAQ particles are better stabilized; therefore, they are less acidic in the Lewis sense and less readily form the intermolecular bonds.

We succeeded in drawing fibres by the both drawing methods described above. The first method—direct drawing from dry to humid atmosphere from a flask—allowed to pull fibres one by one, from all AQ precursors for the R values listed in table 1, and from the NAQ fractions 4–7 of $Sn(OBu)_4$ concentrates. The fibres had a typical length of 10–50 cm and

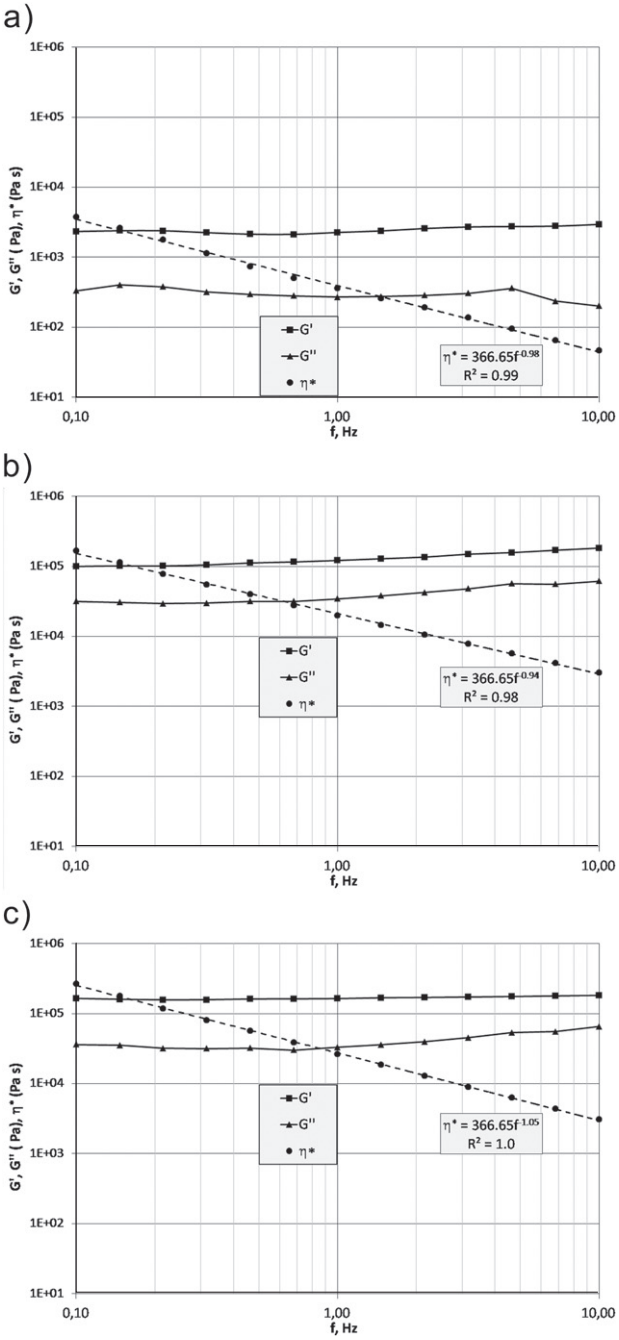

Figure 11. Viscoelastic parameters (η^*; G'; G'') of tin alkoxide systems: (a) $Sn(OBu)_4$, (b) AQ-treated $Sn(OBu)_4$ and (c) NAQ-treated $Sn(OBu)_4$.

a diameter of 1–50 μm depending on the amount of material used for the drawing. Suitable pulling speeds were limited to 1–10 m s^{-1}. Microscopic images of the fibres are shown in figure 12.

The second method, i.e. pulling in dry atmosphere, typically resulted in a simultaneous formation of 10–100 fibres of different diameters. Because of the spread in the initial amount of material the fibre diameters varied widely, from 200 nm to 10 μm. The minimum diameter was 500 nm for the AQ-treated samples and 200 nm for the NAQ fractions 4 and 5, and the diameters were more uniform for the NAQ

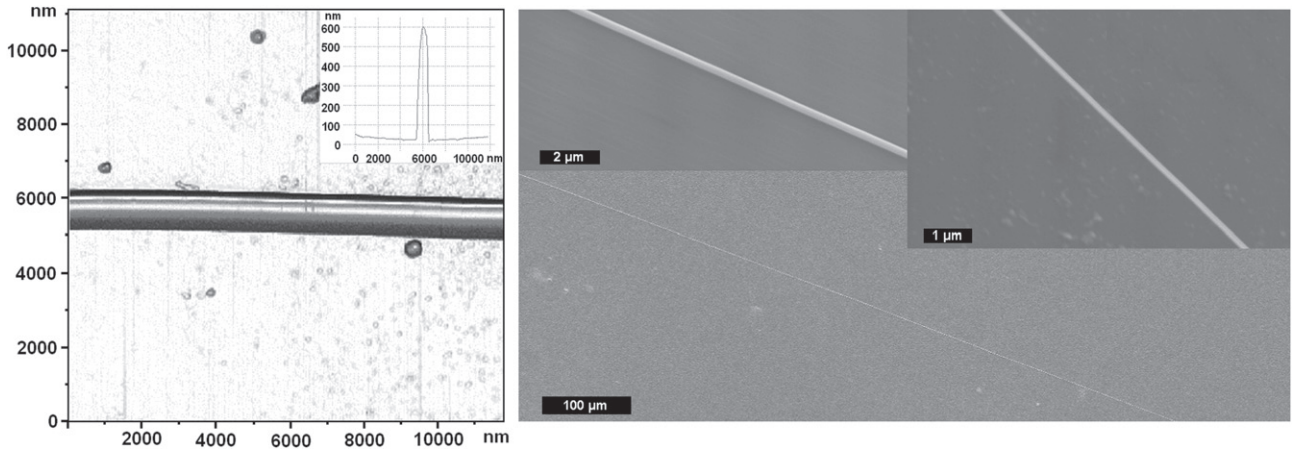

Figure 12. AFM (left) and SEM (right) images of SnO_2 fibres obtained from NAQ-treated $Sn(OBu)_4$ precursors. The inset of the left image shows an AFM line profile of a fibre layng on the substrate. Images are taken after heat treatment.

fibres. The respective aspect ratios were 1000 and 10 000 for the AQ and NAQ precursors, respectively. The better performance of the NAQ precursors could be explained by their higher elasticity compared to the AQ precursors. The smaller minimum diameter relates to the lower surface tension of the NAQ precursors, which also lead to the break-up of the jets. Another reason is the higher chemical stability of the NAQ precursors that allows prolonged fibre drawing in air before the onset of solidification.

In good agreement with [46], the cross-section of our fibres was always strictly circular owing to the use of highly concentrated precursors. AFM imaging over a 5 μm distance along the fibre axis revealed a surface roughness of 1–2 nm or less, that is at the atomic level (figure 12).

3.4. Post-treatment of the fibres

Fibres thinner than 50 μm usually survived the ageing and heat treatment without cracking. The heat treatment oxidized and removed organic components resulting in a volume loss of about 40%. Fibres thinner than a few microns did not crack during the heating even if they were supported by a substrate. This could be explained by a decrease in diameter while the length remained unchanged, that is, the fibres behaved similarly to substrate-supported thin films, which reduce their thickness upon heating and eventually crack. Most of fibres remained visually transparent during the processing, except for the dark brown CeO_2 fibres.

3.5. Waveguiding properties and possible photonics applications of the fibres

Fairly efficient coupling of light was achieved for relatively thick fibres (>10 μm) light simply by focusing a laser beam onto their ends. However, evanescent coupling was several times far more efficient for thinner fibres (2–3 μm in diameter). Such coupling could not always be established, probably because only a few modes could be excited for fibres as thin as the wavelength of light. Therefore, the resonance between sol–gel fibres and silica fibres of different diameters and refractive indices could be achieved only occasionally.

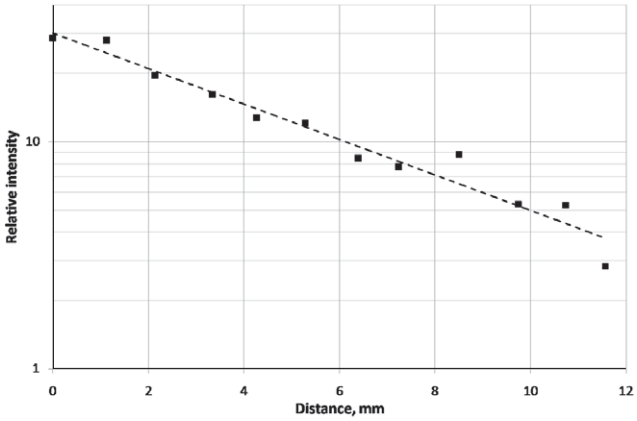

Figure 13. Attenuation of 532 nm laser light propagating within a sol–gel-prepared ZrO_2 fibre of 3 μm diameter. The fit (dashed line) corresponds to a loss of 0.8 dB mm^{-1}.

Figure 13 shows typical waveguiding characteristics of as-prepared AQ fibres few microns in diameter. The losses generally remained below 1 dB mm^{-1}. The attenuation is comparable to the reported losses in sol–gel-derived metal-oxide planar waveguides [47, 48]. Similar losses were also reported for silica nanofibres [25] and SnO_2 nanoribbons [49], but it is unclear whether the observed losses can be maintained in nanometre-thin sol–gel fibres—the downscaling demands higher fibre uniformity; on the other hand, better quality can be expected for the sol–gel-derived nanofibres. The diameter has a marked impact on the waveguiding ability at the microscale as the fibres thicker than 10 μm had nearly undetectable losses.

The marked increase of losses with decreasing fibre diameter is usually attributed to the surface roughness and diameter variations [50]. However, AFM and SEM results suggest that these contributions are inessential in our fibres. Surface contamination could be more important here considering that a higher fraction of the electromagnetic energy is propagating in the evanescent field at lower fibre diameters. In addition, bulk defects added to the fibres during the preparation (such as dust particles) may affect thin fibres.

Nevertheless, good light propagation properties achieved for thick fibres and the excellent surface quality suggest the suitability of the sol−gel route for preparing nanofibres for integrated photonic devices.

4. Conclusions

Metal oxide fibres with a high aspect ratio of up to 10 000 have been drawn from concentrated metal alkoxide precursors. The fibre diameter could be as small as 200 nm, reaching the limit for polymer systems. Rheological tests proved that the metal alkoxide precursors behave as typical non-Newtonian fluids. The observed shear thinning flow behaviour was explained by the formation of linear supramolecular aggregates in the material, which slide under external stress similarly to polymer particles in shear thinning systems.

The best fibre drawing performance, including the highest uniformity and smallest diameter, was achieved for the NAQ precursors and attributed to their higher elasticity compared to the conventional AQ precursors. The preparation of thinner fibres is also promoted by the lower surface tension and higher chemical stability of the NAQ precursors, so that fibres can be drawn for a longer time in air before solidification occurs. XRD measurements revealed 1 nm cassiterite particles in the NAQ precursors whereas the AQ precursors were amorphous. ^{119}Sn NMR results reflected the regularity of the structures and a decrease of Sn coordination from 6 to 5 during the NAQ precursor preparation. FTIR spectra of the NAQ precursors showed characteristic changes in the range 400−600 cm^{-1}, which correspond to the stretching vibrations of the Sn–O bond. SAXS analysis supported earlier reports of the formation of nanometre-sized particles in the first stages of condensation. DAMMIN modelling suggested an elongated particle shape, which could be explained by a unidirectional agglomeration of 2–3 nanoparticles.

The chemical processes occurring during the fibre preparation involve formation of metal–oxygen–metal bonds. The uniform nanostructure of our precursors resulted in solid fibres with excellent properties such as high homogeneity and low surface roughness. The structural uniformity ensures acceptable waveguiding properties of the fibres, and the losses in the ZrO_2 fibres of 3 μm diameter were smaller than 1 dB mm^{-1}. It was possible to densify the structure and to burn out organic components from all the studied materials. The fibres did not crack during the heating even when they were thinner than a few microns and were supported by a solid substrate. These results open future perspectives of direct drawing of metal oxide fibres for integrated optoelectronic devices.

Acknowledgments

The work was supported by the Estonian Science Foundation (grant nos. 7603, 8377, 7612, JD69, JD120, SF0180073s07 and SF0180058s07) and ESF FANAS program NANOPARMA. We thank Dr Chris Pipe for fruitful discussions on the rheology of non-Newtonian liquids and Professor Vadim Kessler for discussions about metal-oxo-alkoxide structures.

References

[1] Ullmann F 2008 *Ullmann's Fibers* (Weinheim: Wiley-VCH)
[2] Rodriguez F 2003 *Principles of Polymer systems* 5th edn (London: Tailor and Francis)
[3] Tätte T, Paalo M, Kisand V, Reedo V, Kartushinsky A, Saal K, Mäeorg U, Lõhmus A and Kink I 2007 *Nanotechnogy* **18** 124501
[4] Ziabicki A and Taksermann-Krozer R 1964 *Koll. Zeits. u. Zeits. Polym.* **198** 60
[5] Ondarçuhu T and Joachim C 1998 *Europhys. Lett.* **42** 215
[6] Li D and Xia Y 2004 *Adv. Mater.* **16** 1151
[7] Ajayan P M, Schadler L S and Braun P V 2003 *Nanocomposite Science and Technology* (Weinheim: Wiley-VCH)
[8] Sakka S and Yoko T J 1992 *Non-Crystal. Solids* **147–148** 394
[9] Bunsell A R and Berger M-H 1999 *Fine Ceramic Fibres* (NewYork: Marcel Dekker)
[10] Kallala M, Sanchez C and Cabane B 1993 *Phys. Rev.* E **48** 3692
[11] Livage J, Henry M and Sanchez C 1988 *Prog. Solid State Chem.* **18** 259
[12] Kessler V and Seisenbaeva G A 2008 *Sol–Gel Methods for Materials Processing* ed P Innocenzi *et al* (Berlin: Springer) p 139
[13] Kessler V 2009 *J. Sol–Gel Sci. Technol.* **51** 264
[14] Turova N Y 2004 *Russ. Chem. Rev.* **73** 1041
[15] Niederberger M and Garnweitner G 2006 *Chem. Eur. J.* **12** 7282
[16] Klein L 1994 *Sol–Gel Optics: Processing and Applications* (Dordrecht: Kluwer)
[17] Sakka S 2005 *Handbook of Sol–Gel Science and Technology: Processing, Characterization, and Applications* (Dordrecht: Kluwer)
[18] Zelinski B J J and Uhlmann D R 1984 *Phys. Chem. Solids* **45** 1069
[19] Andrianov K A 1965 *Metalorganic Polymers* (New York: London, Sydney: Wiley)
[20] Rinse J 1964 *Ind. Eng. Chem.* **56** 42
[21] Nesmeyanov A N, Braynina E M and Freydlina R K 1952 *Dokl. Akad. Nauk SSSR* **85** 571
[22] Ams M, Marshall G D, Dekker P, Dubov M, Mezentsev V K, Bennon I and Withford M J 2008 *IEEE J. Sel. Top. Quantum Electron.* **14** 1370
[23] Phalippou J 2002 *C. R. Chim.* **5** 855
[24] Mizuno T, Nagata H and Manabe S J 1988 *Non-Crystal. Solids* **100** 236
[25] Tong L, Gattass R R, Ashcom J B, He S, Lou J, Shen M, Maxwell I and Mazur E 2003 *Nature* **426** 816
[26] Nain A, Wong J, Amon C and Sitti M 2006 *Appl. Phys. Lett.* **89** 183105
[27] Rao C N R, Deepak F L, Gundiah G and Govindaraj A 2003 *Prog. Solid State Chem.* **31** 5
[28] Xia Y N, Yang P D, Sun Y G, Wu Y Y and Mayers B 2003 *Adv. Mater.* **15** 353
[29] Kuchibhatla S V N T, Karakoti A S, Bera D and Seal S 2007 *Prog. Mater. Sci.* **52** 699
[30] 1976 U.S. Patent 3946056
[31] Gradeff P S, Schreiber F G, Brooks K C and Sievers R G 1985 *Inorg. Chem.* **24** 1110
[32] Maire J-C 1961 *Ann. Chim.* **6** 969
[33] Christian S D, Slagle A R, Tucker E E and Scamehorn J F 1998 *Langmuir* **14** 3126
[34] Mändar H, Felsche J, Mikli V and Vajakas T J 1999 *Appl. Crystallogr.* **32** 345
[35] Feigin L A and Svergun D I 1987 *Structure Analysis by Small-Angle X-ray and Neutron Scattering* (New York: Plenum)
[36] Konarev P V, Petoukhov M V, Volkov V V and Svergun D I J 2006 *Appl. Crystallogr.* **39** 277

[37] Tong L, Hu L, Zhang J, Qiu J, Yang Q, Lou J, Shen Y, He J and Ye Z 2006 *Opt. Express* **14** 82
[38] Sirbuly D J, Law M, Pauzauskie P, Yan H Q, Maslov A V, Knutsen K, Ning C Z, Saykally R J and Yang P D 2005 *Proc. Natl. Acad. Sci. USA* **102** 7800
[39] Bradley D C, Caldwell E V and Wardlaw W J 1957 *Chem. Soc.* **79** 4775
[40] Isihara A 1992 *Polymer* **33** 111
[41] Bradley D C and Carter D G 1962 *Can. J. Chem.* **40** 15
[42] Bradley D C, Mehrotra R C, Rothwell I P and Singh A 2001 *Alkoxo and Aryloxo Derivatives of Metals* (NewYork: Academic)
[43] Scott R W J, Coombs N and Ozin G A 2003 *J. Mater. Chem.* **13** 969
[44] Hampden-Smith M J, Wark T A and Brinker C J 1992 *Coord. Chem. Rev.* **112** 81
[45] Ponton A, Barboux-Doeuff S and Sanchez C 1999 *Colloids Surf.* A **162** 177
[46] Sakka S and Kamiya K 1984 *Mater. Sci. Res.* **17** 83
[47] Urlacher C, Marco de, ucas C, Bernstein E, Jacquier B and Mugnier J 1999 *Opt. Mater.* **12** 19
[48] Mechiakh R, Meriche F, Kremer R, Bensaha R, Boudine B and Boudrioua A 2007 *Opt. Mater.* **30** 645
[49] Sirbuly D J, Law M, Pauzauskie P, Yan H Q, Maslov A V, Knutsen K, Ning C Z, Saykally R J and Yang P D 2005 *Proc. Natl. Acad. Sci. USA* **102** 7800
[50] Sumetsky M 2006 *Opt. Lett.* **31** 870